PLOS ONE

Extracellular electrical conductivity property imaging by decomposition of high-frequency conductivity at Larmor-frequency using multi-*b*-value diffusion-weighted imaging

Mun Bae Lee[1], Geon-Ho Jahng[2], Hyung Joong Kim[3], Eung Je Woo[3], Oh In Kwon[1] *

1 Department of Mathematics, Konkuk University, Seoul, Korea, **2** Department of Radiology, Kyung Hee University Hospital at Gangdong, College of Medicine, Kyung Hee University, Seoul, Korea, **3** Department of Biomedical Engineering, Kyung Hee University, Seoul, Korea

* oikwon@konkuk.ac.kr

Abstract

Magnetic resonance electrical properties tomography (MREPT) uses the B1 mapping technique to provide the high-frequency conductivity distribution at Larmor frequency that simultaneously reflects the intracellular and extracellular effects. In biological tissues, the electrical conductivity can be described as the concentration and mobility of charge carriers. For the water molecule diffusivity, diffusion weighted imaging (DWI) measures the random Brownian motion of water molecules within biological tissues. The DWI data can quantitatively access the mobility of microscopic water molecules within biological tissues. By measuring multi-*b*-value DWI data and the recovered high-frequency conductivity at Larmor frequency, we propose a new method to decompose the conductivity into the total ion concentration and mobility in the extracellular space (ECS) within a routinely applicable MR scan time. Using the measured multi-*b*-value DWI data, a constrained compartment model is designed to estimate the extracellular volume fraction and extracellular mean diffusivity. With the extracted extracellular volume fraction and water molecule diffusivity, we directly reconstruct the low-frequency electrical properties including the extracellular mean conductivity and extracellular conductivity tensor. To demonstrate the proposed method by comparing the ion concentration and the ion mobility, we conducted human experiments for the proposed low-frequency conductivity imaging. Human experiments verify that the proposed method can recover the low-frequency electrical properties using a conventional MRI scanner.

Introduction

Using a magnetic resonance imaging (MRI) scanner, various techniques to measure and analyze the electrical properties of biological tissue have been developed and experimented [1–7]. The passive electrical properties of biological tissues appear complex phenomenon, depending

on various factors, such as frequency, ion mobility, ion concentration, cell shapes, and cell membranes, etc. In biological tissues, frequency-dependent electrical properties such as permittivity and conductivity are divided into two electrically conducting compartments: the intracellular and extracellular spaces due to the cell membrane resistance, depending on frequency. The measurement of electrical conductivity of brain tissue has been initiated in the 1960s. Due to the insulation properties of thin cell membranes, internal electrical current flow caused by external current stimulation at low-frequency reflects ECS and cerebrospinal fluid (CSF), excluding the intracellular space (ICS). [1, 8, 9].

Magnetic resonance electrical impedance tomography (MREIT) has been developed to visualize electrical conductivity and/or current density images at low frequencies (below 1 kHz) by directly injecting low-frequency current through attached electrodes on the surface of imaging object [2, 4, 10, 11]. In MREIT, one component of the induced magnetic flux density is acquired using an MRI scanner. Most MREIT algorithms have focused on visualizing the isotropic conductivity distribution by using only one component of the magnetic flux density data [12–14]. Combining the diffusion tensor imaging (DTI) and MREIT techniques, DT-MREIT method, which is a direct method for absolute conductivity tensor image, was proposed based on the linear relationship between the water diffusion tensor and the electrical conductivity tensor [3, 15]. MREIT technique is a direct method to investigate the internal low-frequency electrical properties, however, various difficulties still need to be overcome due to the external direct current injection into the human body.

For the high-frequency conductivity using a conventional MRI scanner without any external electrical stimulation, magnetic resonance electrical properties tomography (MREPT) techniques successfully recover the conductivity distribution at Larmor frequency (about 128 MHz at 3 T) [7, 16, 17]. Since the electrical conductivity of biological tissues is primarily determined by the concentration and mobility of ions, the electrical conductivity can be sensitive to the changes of physiological and pathological conditions of tissues and organs [16]. A recent work using MREPT technique shows that the recovered high-frequency electrical conductivity is sensitive to microstructural changes of tissues due to irradiation [18].

Using the B1 mapping technique, the high-frequency electric conductivity at Larmor frequency, which simultaneously reflects the combined electrical properties in ICS and ECS, can be formally decomposed into a two compartment conductivity model specific to ICS and ECS. In each compartment, the electrical conductivity can be expressed as the product of concentration and mobility of charge carriers such as ions and charged molecules. In the case of biological tissue containing the intracellular and extracellular fluids, the extracellular matrix material and the cells with insulating membrane also contribute to the conductivity of biological tissues [19].

Diffusion-weighted imaging (DWI), based on the diffusion of water molecules in tissues, provides potentially information on the brain functional activity, *in vivo* and non-invasively. Multi-*b*-value DWIs can probe the microstructure of neural tissues and analyze its hindrance to water diffusion using various signal models [20–24]. Intravoxel incoherent motion (IVIM) imaging is a model for evaluating the diffusion procedure in biological tissues using a bi-exponential model [20, 21]. The bi-exponential model is based on the assumption that the slow diffusion is attributed to water molecules interacting with the cell membranes and associated cell structures, while the fast diffusion component occur in less restricted water environments found in both intracellular and extracellular spaces. Both slow and fast water pools may coexist in the intracellular compartment.

Lately, an electrodeless method providing the low-frequency conductivity tensor image (LF-CTI) using a clinical MRI scanner without any external hardware has been initiated [25, 26]. The proposed LF-CTI method based on the observation that the conductivity is

proportional to the product of mobility and concentration of charge carriers. Since MREPT technique can recover the high-frequency conductivity at Larmor-frequency, the LF-CTI method mainly focuses on separating the ion mobility and concentration in ECS from the recovered high-frequency conductivity.

The LF-CTI method provides a possible way to visualize the low-frequency conductivity tensor map without additional external injection current, human imaging experiments, however, were deferred mainly due to lack of validation studies. The LF-CTI method needs to overcome several difficulties [25, 26]:

- To separate the recovered high-frequency conductivity into the intracellular and extracellular compartments, the LF-CTI method solved a three compartment model to estimate the extracellular volume fraction and diffusion coefficients in ECS and ICS. The determination of diffusion coefficients and extracellular volume fraction from the three pool model, that is a combination of multi-exponential curves, is highly sensitive to the measured noise.

- DWI signals reflected the effects of ICS and ECS, but the LF-CTI method used the diffusion tensor at $b = 800$ s/mm^2 as the extracellular diffusion tensor.

- The LF-CTI method requires a relatively long MR scan time due to the number of diffusion gradients and multi-b-value DWIs.

We propose a method to provide a low-frequency electrical conductivity property imaging using B1 phase map and multi-b-value DWI data (MbD-LF-CPI). The proposed MbD-LF-CPI method separates the apparent extracellular ion concentration and mobility, acquired within clinically applicable MR scan time. With an additional diffusion tensor at a fixed b-value, a method for the low-frequency conductivity tensor imaging is also proposed.

We introduce a new multi-compartment model to stably extract the extracellular mean diffusivity, extracellular volume fraction, and isotropic volume fraction, which are parameters related to multi-b-value DWIs. The proposed method is motivated by the neurite orientation dispersion and density imaging (NODDI), a widely used model to infer microstructural features in the brain [23]. NODDI uses three types of microstructural environment (intra-neurite, extra-neurite, and CSF) to estimate a neurite density index (NDI) and an orientation dispersion index (ODI). NODDI requires multiple b-values and many diffusion gradient directions. The anisotropic intra-neurite compartment was modeled as a set of sticks, assuming unhindered diffusion along the neurite to capture the highly restricted diffusion properties [27, 28].

The relatively long acquisition time for NODDI characterizing the dispersion and density has been the limitation for clinical applications due to high scan costs. To separate low-frequency conductivity from the high-frequency conductivity, the proposed method only needs the extracellular volume fraction and diffusion coefficient, not the orientation dispersion recovered from a conventional NODDI. To characterize the total ion concentration weighted part in the brain region, we reasonably assume that the mobility of charge carriers is proportional to that of water molecules in the same structural environment. The proposed model includes three unknowns to be determined such as extracellular volume fraction, extracellular mean diffusivity, and isotropic volume fraction. With the high-frequency conductivity and the estimated parameters using the proposed model, we reconstruct the low-frequency mean conductivity.

After the determination of low-frequency mean conductivity, using the estimated extracellular diffusivity and the measured water diffusion tensor at a fixed b-value, to extract the low-frequency anisotropic electrical properties, we propose a method of separating the diffusion tensor at a fixed b-value into the intracellular and extracellular diffusion tensors.

To demonstrate the proposed method, we conducted human experiments and recovered the high-frequency conductivity using the measured B1 phase map. For MREPT experiments, a multi-spin-echo pulse sequence with multiple refocusing pulses was used to reduce measured noise artifact. Since measured multi-b-value DWIs exponentially decayed, it is difficult to avoid the noise amplification from the three compartment model even with 15 b-values [25]. To quantitatively compare the quality of reconstructed parameters, we used 7 and 4 b-value DWIs to extract the microstructural parameters such as the volume fraction and mean diffusivity in ECS. The extracellular diffusion tensor map was recovered through the estimated extracellular diffusivity and the measured diffusion tensor map at a fixed b-value. The low-frequency conductivity tensor was recovered using the extracellular diffusion tensor map, the microstructural parameters with multi-b-value DWIs, and high-frequency conductivity. The human experiments verified that the proposed method has the potential to rapidly recover the low-frequency electrical properties without any additional external injection current.

Materials and methods

Preliminary

High-frequency conductivity using B1-map. The high-frequency electrical tissue properties of conductivity σ_H and permittivity ϵ_H satisfy the following at Larmor frequency ω

$$\nabla^2 \mathbf{B}_1 = i\omega\mu_0\gamma_H\mathbf{B}_1 - \frac{\nabla\gamma_H}{\gamma_H} \times (\nabla \times \mathbf{B}_1)$$

where $\gamma_H = \sigma_H + i\omega\epsilon_H$, $\mathbf{B}_1$ denotes the B1 field and $\mu_0 = 4\pi \times 10^{-7}$ N/A^2 is the magnetic permeability of free space [7]. For the positive (negative) rotating component of the transmit B1 field $B_1^+ = |B_1^+|e^{i\phi^+}$ ($B_1^- = |B_1^-|e^{i\phi^-}$), by assuming $\sigma_H \gg \omega\epsilon_H$, a phase-based convection reaction equation-based MREPT formula was derived as

$$\left(\nabla\phi^{tr} \cdot \nabla\left(\frac{1}{\sigma_H}\right)\right) + \frac{\nabla^2\phi^{tr}}{\sigma_H} - 2\omega\mu_0 = 0 \tag{1}$$

where $\phi^{tr} = \phi^+ + \phi^-$ is the transceiver phase using MRI [6]. To stabilize the formula (1), after adding an artificial diffusion term, the Eq (1) leads to

$$-c\nabla^2\left(\frac{1}{\sigma_H}\right) + \left(\nabla\phi^{tr} \cdot \nabla\left(\frac{1}{\sigma_H}\right)\right) + \frac{\nabla^2\phi^{tr}}{\sigma_H} = 2\omega\mu_0 \tag{2}$$

where c is a constant diffusion coefficient.

Multi-b-value DWI. In DWI, two magnetic field gradients with the same area between 180˚ RF pulse are used. The first gradient induces dephasing of water proton spins and the second gradient refocuses the spins. The amount of diffusion weighting can be controlled by modifying the b-value, which is related with the gradient area, strength, and time spacing between the two magnetic filed gradients. The signal intensity S_j by applying a diffusion encoding gradient is given by

$$S_j = S_0 \exp(-b_j D), \quad j = 1, \cdots, N_b$$

where S_0 is the signal obtained without diffusion gradient and b_j denotes the diffusion-weighting factor depending on the gradient pulse used in the DWI sequence:

$$b_j = \gamma^2\delta_j^2 G_j^2\left(\Delta_j - \frac{\delta_j}{3}\right)$$

where $\gamma = 26.75 \times 10^7\ rad/Ts$ is the gyromagnetic ratio of hydrogen, Δ_j is the diffusion time interval, and δ_j and G_j are the duration and amplitude, respectively, of the diffusion-sensitizing gradient pulse along a given direction.

Decomposition of high-frequency conductivity σ_H. Biological tissues contain several charge carriers. K^+, Na^+, Ca^{2+}, Cl^-, and several ions are dominant charge carriers in the extracellular and intracellular fluids. Using the Einstein relation between the diffusivity and mobility of charge carriers, the electrical mobility m_j of the j-th charge carrier in biological tissues can be expressed as

$$m_j = \left(\frac{q}{k_B T}\right)d_j = \left(\frac{r_w q}{r_j k_B T}\right)d_w$$

where $q = 1.6 \times 10^{-19}$C is the absolute value of the charge of electron, k_B is the Boltzmann constant, r_w and r_j are the Stokes radius of a water molecule and an ion, respectively, d_w is the diffusion coefficient of a water molecule, and T is the absolute temperature.

The diffusion coefficient d_w is related to the medium viscosity and Stokes radius of the water molecule. Using the relation between the apparent conductivity σ_a and diffusion coefficient, the apparent electrical conductivity in the biological tissues can be represented as

$$\sigma_a = \sum_{j=1}^{N_E} c_j m_j = \sum_{j=1}^{N_E} c_j \left(\frac{r_w q}{r_j k_B T}\right)d_w = \bar{c}_a d_w$$

where c_j denotes the concentration of the j-th ion. In this paper, we set $\bar{c}_a = \sum_{j=1}^{N_E} c_j \left(\frac{r_w q}{r_j k_B T}\right)$ as the apparent total ion-concentration for the water molecule.

The reconstructed high-frequency conductivity can be decomposed into the extracellular and intracellular compartments:

$$\begin{aligned}
\sigma_H &= \sigma_L + \sigma_I \\
&= \alpha \bar{c}_e d_w^e + (1 - \alpha)\bar{c}_i d_w^i
\end{aligned} \tag{3}$$

where α denotes the extracellular volume fraction in a voxel and $\bar{c}_e = \sum_{j=1}^{N_e} c_j^e \left(\frac{r_w q}{r_j k_B T}\right)$, $\bar{c}_i = \sum_{j=1}^{N_i} c_j^i \left(\frac{r_w q}{r_j k_B T}\right)$, and d_w^e and d_w^i are the water diffusion coefficients in ECS and ICS, respectively. Here, the low-frequency conductivity $\sigma_L = \alpha \bar{c}_e d_w^e$ denotes the extracellular conductivity.

Microstructural parameters using multi-b-value DWIs

To investigate the microstructure of biological tissues using the diffusion related parameters obtained from multi-b-value DWIs, the most common method is DTI, which describes diffusion coefficients by a 3×3 symmetric matrix. The bi-tensor model has been solved by increasing the number of diffusion gradients and multi-b-value DWIs, at the cost of long scan time [29]. Multi-compartment models are typically used to eliminate CSF contamination in NODDI [23]. Intravoxel incoherent motion (IVIM) is also a method using multi-b-value DWIs to extract information about the microcirculation and microvasculature in addition to the diffusion parameters:

$$S_j = S_0(f_b \exp\left(-b_j(D_1 + D^*)\right) + (1 - f_b)\exp\left(-b_j D_2\right)) \tag{4}$$

where f_b is the perfusion fraction, D^* is the psedo-diffusion coefficient, D_1 is the water diffusion coefficient in blood, and D_2 is the water diffusion coefficient in the tissue [21]. The pseudo-diffusion coefficient D^* describes the incoherent motion of blood within the capillary network.

Since the perfusion fraction f_b includes the intracellular diffusivity component, the two-compartment model in (4) is not appropriate to extract the low-frequency conductivity component from the recovered high-frequency conductivity σ_H in (3).

NODDI estimates the neurite orientation and dispersion parameters by distinguishing the brain tissue with three types of microstructural compartments: CSF, anisotropic hindered diffusion (extra-neurite space), and anisotropic restricted diffusion (intra-neurite space) [23]. NODDI uses the following three compartment model:

$$A = (1 - v_{iso})(v_{ic}A_{ic} + (1 - v_{ic})A_{ec}) + v_{iso}A_{iso} \tag{5}$$

where A_{ic} and v_{ic} are the normalized signal from water restricted by a directionally orientated cylinder and intra-neurite volume fraction, respectively; A_{ec} is the normalized signal of the extra-neurite compartment and A_{iso} and v_{iso} are the normalized signal and the volume fraction of the CSF compartment, respectively. A_{ic} is represented as

$$A_{ic} = \int_{S^2} \rho(\vec{n})e^{-bd_{\parallel}(\vec{q}\cdot\vec{n})^2} d\vec{n} \tag{6}$$

where ρ is the spherical function that is non-negative, antipodal symmetry, and integrates to 1 over the unit sphere, $\vec{q}$ is the gradient direction, and $\vec{n}$ is an outward unit vector. $e^{-bd_{\parallel}(\vec{q}\cdot\vec{n})^2}$ denotes the signal from water restricted by a stick with diffusivity $d_{\parallel}$ and orientation $\vec{n}$ [23]. To estimate the orientation dispersion index, which is a component of $\rho(\vec{n})$, NODDI requires relatively many gradient directions to cover the unit sphere S^2.

The anisotropic intra-neurite compartment is modeled as a set of sticks to capture the highly restricted diffusion property, which is unhindered diffusion along neurites. The extra-neurite compartment refers to the space hindered by the presence of neurites. The CSF compartment is modeled as isotropic Gaussian diffusion with diffusivity d_{iso}. NODDI uses *a priori* model parameters to stabilize the reconstruction procedure; intrinsic free diffusivity for the intra-neurite $d_{\parallel}(= d_{ic}) = 1.7 \times 10^{-3} \text{mm}^2/\text{s}$ and $d_{iso} = 3.0 \times 10^{-3} \text{mm}^2/\text{s}$ [23].

The NODDI has a sufficient potential as a practical medical image, but still has a problem in clinical applications due to high scan costs. It is important to reduce a number of DWIs to fill the q-space with different diffusion weights and gradient directions. From the point of view of electrical conductivity, a goal is to separate low-frequency conductivity component, $\sigma_L = \alpha\bar{c}_e d_w^e$ in (3), from the high-frequency conductivity σ_H. By modifying the NODDI model to only extract the volume fractions v_{ic} and v_{iso} in (5), and the extracellular mean diffusivity, to extract the low-frequency conductivity component, we propose a multi-compartment model only depending on multi-b-value DWIs:

$$\begin{aligned}\hat{S}_j/S_0 &= (1 - v_{iso})(v_{ic}\exp{(-b_j v_{ic}d_{ic})}\\&\quad + (1 - v_{ic})\exp{(-b_j(1 - v_{ic})d_*^e)})\\&\quad + v_{iso}\exp{(-b_j d_{iso})} + v_0, \quad j = 1, \cdots, N_b\end{aligned} \tag{7}$$

where $d_{ic} = 1.7 \times 10^{-3}\text{mm}^2/\text{s}$ and $d_{iso} = 3.0 \times 10^{-3}\text{mm}^2/\text{s}$. The proposed model includes four unknowns: intracellular volume fraction v_{ic}, extracellular diffusivity $(1 - v_{ic})d_*^e$, isotropic volume fraction v_{iso}, and offset value v_0. By solving the following nonlinear least square problem, we can determine the parameters to separate the intracellular and extracellular compartments:

$$\min_{v_{ic}, d_*^e, v_{iso}, v_0} \| \vec{S} - \hat{\vec{S}}(v_{ic}, d_*^e, v_{iso}, v_0) \|$$

where $\vec{S} = (S_1, \cdots, S_{N_b})$ is the measured DWI signals for multi-b-value DWIs and

$\vec{\hat{S}}(v_{ic}, d_*^e, v_{iso}, v_0) = (\hat{S}_1, \cdots, \hat{S}_{N_b})$ denotes the generated DWI signals by using the proposed compartment model (7).

The extracellular volume fraction α in (3) is estimated at each voxel as

$$\alpha = (1 - v_{iso})(1 - v_{ic}) + v_{iso} \qquad (8)$$

Using the relation, $\alpha d_w^e = (1 - v_{iso})(1 - v_{ic})(1 - v_i)d_*^e + v_{iso}d_{iso}$, the extracellular mean diffusivity can be estimated as

$$d_w^e = \frac{(1 - v_{iso})(1 - v_{ic})^2 d_*^e}{(1 - v_{iso})(1 - v_{ic}) + v_{iso}} + \frac{v_{iso}d_{iso}}{(1 - v_{iso})(1 - v_{ic}) + v_{iso}}$$

The intracellular mean diffusivity is expressed as

$$d_w^i = v_{ic}d_{ic}$$

Low-frequency mean conductivity

To estimate the ratio of ion concentrations in ICS and ECS, for the human brain, the ratio value $\beta = \dfrac{\bar{c}_i}{\bar{c}_e} = 0.41$ was suggested by adopting reference values of intracellular and extracellular ion concentrations of four predominant ions (Na^+, Cl^-, K^+, and Ca^{2+}) [25, 26]. Using the reference ratio value $\beta = 0.41$, the apparent extracellular ion concentration $\bar{c}_e$ can be estimated as

$$\bar{c}_e = \frac{\sigma_H}{\alpha d_w^e + (1 - \alpha)\beta d_w^i} \qquad (9)$$

By subtracting the intracellular compartment of σ_H, the low-frequency mean conductivity, σ_L, is expressed as

$$\sigma_L = \alpha \frac{\sigma_H}{\alpha d_w^e + (1 - \alpha)\beta d_w^i} d_w^e$$

Low-frequency anisotropic conductivity tensor using the relationship between extracellular mean diffusivity and extracellular diffusion tensor

The measured diffusion tensor $\mathbf{D}_b$ at a fixed b-value can be written as a positive definite symmetric matrix:

$$\mathbf{D}_b = \mathcal{S}_D \tilde{\mathbf{D}}_b \mathcal{S}_D^T \quad \text{with} \quad \tilde{\mathbf{D}}_b = \begin{pmatrix} d_1^b & 0 & 0 \\ 0 & d_2^b & 0 \\ 0 & 0 & d_3^b \end{pmatrix}$$

where the column vectors of $\mathcal{S}_D$ are the orthonormal eigenvectors of $\mathbf{D}_b$, the superscript T denotes the transpose and $d_1^b \leq d_2^b \leq d_3^b$ are the corresponding eigenvalues.

We separate the apparent diffusion tensor $\mathbf{D}_b$ into the extracellular and intracellular compartments:

$$\mathbf{D}_b = \alpha \mathbf{D}_{ext} + (1 - \alpha)\mathbf{D}_{int}$$

where $\mathbf{D}_{ext}$ and $\mathbf{D}_{int}$ denote the apparent diffusion tensors in ECS and ICS, respectively. By assuming that the diffusion tensors $\mathbf{D}_{ext}$ and $\mathbf{D}_b$ share the eigenvectors, the extracellular diffusion tensor $\mathbf{D}_{ext}$ can be expressed as

$$\mathbf{D}_{ext} = \mathcal{S}_D \tilde{\mathbf{D}}_{ext} \mathcal{S}_D^T \quad \text{with} \quad \tilde{\mathbf{D}}_{ext} = \begin{pmatrix} d_1^{ext} & 0 & 0 \\ 0 & d_2^{ext} & 0 \\ 0 & 0 & d_3^{ext} \end{pmatrix} \tag{10}$$

Using the estimated extracellular mean diffusivity d_w^e and the relation $d_w^e = (d_1^{ext} + d_2^{ext} + d_3^{ext})/3$, we define a scale parameter η as

$$\eta = \frac{3d_w^e}{d_1^b + d_2^b + d_3^b} \tag{11}$$

Under the hypothesis that the extracellular diffusion tensor $\mathbf{D}_{ext}$ and the diffusion tensor $\mathbf{D}_b$ share the eigenvectors, we can determine the extracellular diffusion tensor:

$$\mathbf{D}_{ext} = \eta \mathbf{D}_b \tag{12}$$

From the relation (12), the low-frequency conductivity tensor can be expressed as the following

$$\mathbf{C}_L = \alpha \bar{c}_e \mathbf{D}_{ext} = \alpha \eta \bar{c}_e \mathbf{D}_b \tag{13}$$

where the ion mobility is assumed to be proportional to the water molecule diffusion flow.

Human experiments setup

Two healthy volunteers without a documented history of any disease were recruited. The participants were located inside the bore of a 3T MRI scanner with a 32-channel RF head coil (Achieva TX, Philips Medical Systems, the Netherlands). All experimental protocols were approved by the institutional review board of Kyung Hee University (KHSIRB-16-033). All methods were carried out in accordance with the relevant guidelines and regulations and all participants provided written informed consent.

For MREPT imaging experiments, the multi-spin-echo pulse sequence with multiple refocusing pulses was adopted. Before the data acquisition, we applied a volume shimming method with the volume defined to cover the brain region. Imaging parameters were as follows: repetition time T_R = 1500 ms, echo time T_E = 15 ms, number of echoes (NE) = 6, number of excitation (NEX) = 1, slice thickness = 4 mm, number of slices = 5, acquisition matrix = 128×128, field-of-view (FOV) = 240 × ?240 mm^2, and scan time = 16 min.

DWI data sets were obtained using the single-shot spin-echo echo planner imaging (SS-SE-EPI) pulse sequence [30]. We applied the diffusion weighting gradients in 15 directions with 15 b-values of 50, 150, 300, 500, 700, 1000, 1400, 1800, 2200, 2600, 3000, 3600, 4000, 4500, and 5000 s/mm^2, respectively. Imaging parameters were as follows: T_R = 2000 ms, T_E = 70 ms, flip angle = 90˚, NEX = 2, slice thickness = 4 mm, number of slices = 5, acquisition matrix = 64 × 64 and scan time = 23 min. The matrix size of 64 × 64 was extended to 128 × 128 to match the spatial resolution of MREPT experiment. We used only 3 orthogonal gradient directions in the experiments and the results were also compared to the results estimated using 15 gradient directions.

Fig 1(a) and 1(b) show the MR magnitude and the B1 phase image at the first imaging slice using the spin MR pulse sequence, respectively. Fig 1(c) shows MR magnitude variations
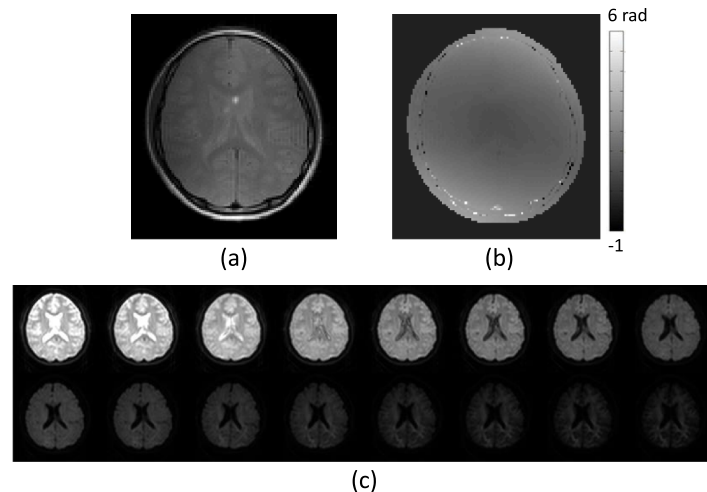
Fig 1. MR magnitude and B1 phase images. (a) MR magnitude image and (b) B1 phase image at the first imaging slice using the spin MR pulse sequence. (c) MR magnitude images corresponding to multi-b-value: b = 0, 50, 150, 300, 500, 700, 1000, 1400, 1800, 2200, 2600, 3000, 3600, 4000, 4500, and 5000 s/mm^2, respectively.

https://doi.org/10.1371/journal.pone.0230903.g001

corresponding to multi-b-values: b = 0, 50, 150, 300, 500, 700, 1000, 1400, 1800, 2200, 2600, 3000, 3600, 4000, 4500, and 5000 s/mm^2, respectively.

Results

Low-frequency mean conductivity

We reconstructed the high-frequency conductivity, σ_H, with the acquired transceiver phases of the B1 maps (Fig 1(b)) by solving the partial differential equation in (3).

To avoid the background phase signal due to the consecutive 180° RF pulses, we used odd echoes of six measured complex signals to reduce measured noise. Since the amount of noise in the phase signal is inversely proportional to MR magnitude intensity, $\tilde{\mathcal{S}}_k$, $k = 1, 3, 5$, the measured phase signal was optimized as a weighted averaging using the weight of [31]

$$w_k = \frac{|\tilde{\mathcal{S}}_k|^2}{|\tilde{\mathcal{S}}_1|^2 + |\tilde{\mathcal{S}}_2|^2 + |\tilde{\mathcal{S}}_3|^2}, \ k = 1, 3, 5$$

Fig 2(a) shows the recovered high-frequency conductivity image in the first imaging slice of the brain. To solve the Eq (2), we discretized using three-point central difference approximation to derive a matrix system $\mathbf{Ax} = \mathbf{b}$ in the brain region. To stabilize the reaction-diffusion Eq (2), we used the diffusion term $c = 0.025$ to estimate the high-frequency conductivity images. The estimated conductivity values were slightly lower than the known reference conductivity values because the evaluation procedure for the conductivity included the numerical differentiations and the regularization parameter c in (2).

Fig 2(b) shows the extracellular volume fraction α, extracellular mean diffusivity d_w^e, intracellular diffusivity d_w^i, apparent extracellular ion concentration $\bar{c}_e$ and low-frequency mean conductivity σ_L, respectively, using the proposed MbD-LF-CPI method.

We designed the diffusion coefficient term in the intracellular compartment by including the intracellular volume fraction information, $\exp(-b_j\, v_{ic}\, d_{ic})$, in (7). Using the high-frequency conductivity and the estimate diffusion parameters, we recovered an apparent extracellular ion
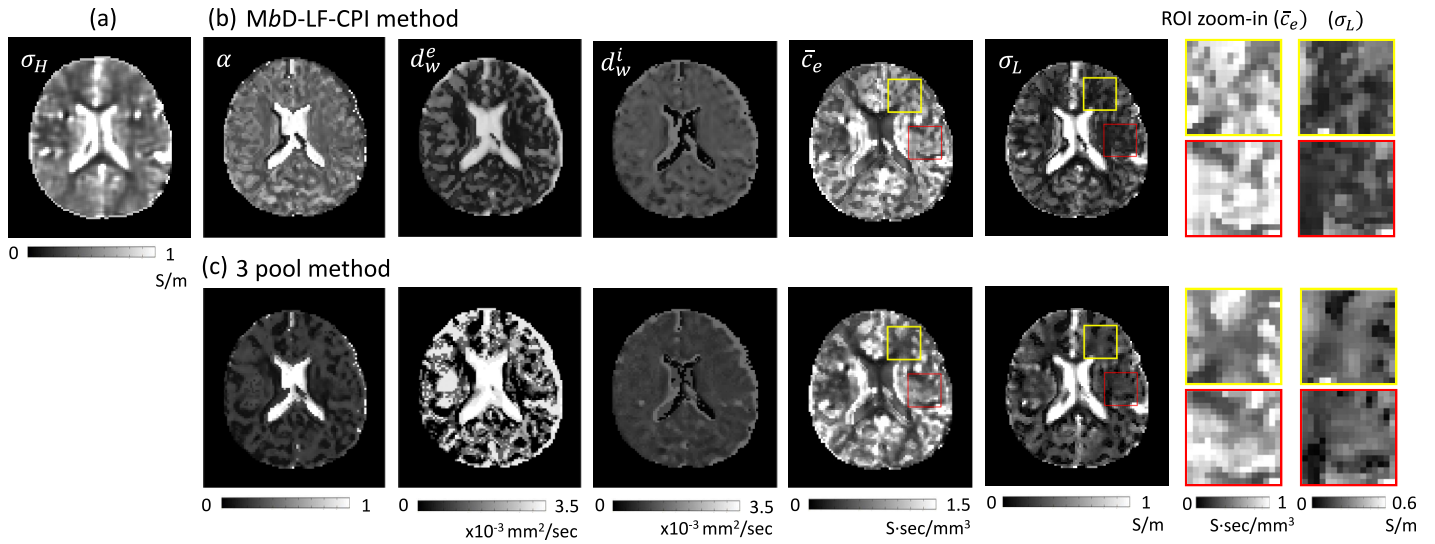
Fig 2. Comparisons of the results using MbD-LF-CPI and the three pool method in (14). (a) Recovered high-frequency conductivity σ_H. (b) Recovered extracellular volume fraction α, extracellular mean diffusivity d_w^e, intracellular diffusivity d_w^i, apparent extracellular ion concentration $\bar{c}_e$ and low-frequency mean conductivity σ_L images, respectively, using MbD-LF-CPI method. (c) Recovered results corresponding to the results in (b) using the three pool model method in (14). To show the difference more clearly, the last two columns zoom in on the area marked by the rectangles.

concentration, $\bar{c}_e$, in (9). The extracellular ion concentration in the white matter region was lower than in other regions, especially in the genu and splenium of the corpus where the density of thin unmyelinated fibers was high. Comparing to the high-frequency conductivity σ_H, the low-frequency mean conductivity σ_L shows different electrical characteristics in Fig 2(b).

Since the given observable multi-b-value DWI data are a combination of exponentially decay signals depending on the diffusion gradient strength, the method of estimating the extracellular volume fraction, intracellular diffusivity and extracellular mean diffusivity is sensitive to the measured noise. Due to the ill-posedness, the first proposed electrodeless method fitted the exponentially decay signals by using the three pool model [25]:

$$\hat{S}_j/S_0 = v_{ecm} \exp\left(-b_j d_{ecm}^w\right) + v_{ecm} \exp\left(-b_j d_{ecw}^w\right) \\ + v_i \exp\left(-b_j d_i^w\right) + v_0, \quad j = 1, \cdots, N_b \tag{14}$$

where $d_{ecw}^w = 3.0 \times 10^{-3} \text{mm}^2/\text{s}$.

Using the three pool model in (14), the extracellular volume fraction α and extracellular diffusion coefficient d_w^e are estimated at each voxel as

$$\alpha = \frac{v_{ecm} + v_{ecw}}{v_{ecm} + v_{ecw} + v_i}$$

and

$$d_w^e = \frac{v_{ecm}}{v_{ecm} + v_{ecw}} d_{ecm}^w + \frac{v_{ecw}}{v_{ecm} + v_{ecw}} d_{ecw}^w.$$

In this paper, we compared the reconstructed results using the proposed method to those using the three pool model in (14): Fig 2(c) shows the results of the three pool method. To show the difference more clearly, the last two columns zoom in on the area marked by the rectangles.
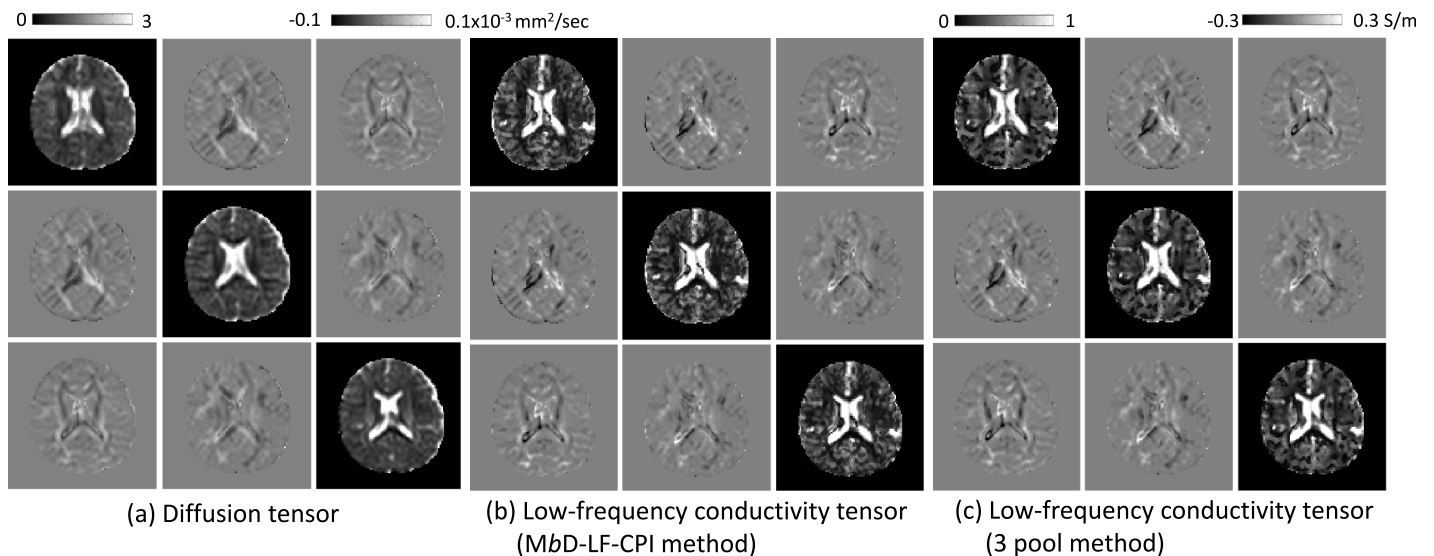
Fig 3. Diffusion and conductivity tensors. (a) Water molecule diffusion tensor using the *b* value of 1000 s/mm² in the first slice. (b) Reconstructed low-frequency conductivity tensor images using the proposed M*b*D-LF-CPI method. (c) Reconstructed low-frequency conductivity tensor images using the three pool model in (14).

Experiment results for the other human subject are included in the supporting information (S1 Fig).

Low-frequency conductivity tensor

Fig 3(a) shows the 3×3 diffusion tensor components using DWIs with *b*-value of 1000 s/mm². To extract the water molecule diffusion tensor in ECS, we solved the Eqs (11) and (12) using the estimated extracellular mean diffusivity d_w^e and the diffusion tensor $\mathbf{D}_b$. From the estimated extracellular diffusion tensor $\mathbf{D}_{ext}$, the extracellular volume fraction $\alpha = (1 - v_{iso})(1 - v_{ic}) + v_{iso}$ in (8), and the extracellular ion concentration $\bar{c}_e = \frac{\sigma_H}{\alpha d_w^e + (1-\alpha)\beta d_w^i}$ in (9), we reconstructed the low-frequency conductivity tensor map $\mathbf{C}_L$ in (13), which was displayed in Fig 3(b).

The estimated low-frequency conductivity tensor using the proposed method was slightly low in the white matter region. Fig 3(c) shows the estimated low-frequency conductivity tensor map corresponding to the three pool method. S2 Fig shows the corresponding results in Fig 3.

To verify the proposed method, the brain region was segmented into CSF, gray matter (GM), and white matter (WM) regions. Table 1(a) shows the estimated high-frequency conductivity, apparent extracellular ion concentration, low-frequency mean conductivity, and the diagonal components of the reconstructed low-frequency conductivity tensor in the segmented ROIs. The conductivity of WM, composed of myelinated nerve axons, is highly anisotropic with different longitudinal and transverse conductivity. Especially, in WM region, the low-frequency conductivity seems to be more hindered. The low-frequency conductivity, estimated in WM region, was relatively smaller than the high-frequency conductivity.

The diagonal components of the diffusion tensor in CSF region were $2.5\pm0.6 \times 10^{-3}$, $2.9 \pm0.7 \times 10^{-3}$, and $2.8\pm0.8 \times 10^{-3}$ mm²/s, respectively. Thus, in CSF region, the second component of the recovered low-frequency conductivity tensor C_{22} was relatively high. The mean of diagonal components of the low-frequency conductivity tensor in CSF was 1.18 ± 0.43 S/m, which was similar to the high-frequency conductivity value 1.19 ± 0.40 S/m in CSF.

Table 1(b) summarizes the results of the three pool method (See also S1 Table).

Table 1. Results of the proposed MbD-LF-CPI method and the three pool method. Estimated high-frequency conductivity σ_H, extracellular ion concentration $\bar{c}_e$, low-frequency mean conductivity σ_L, diagonal components of reconstructed low-frequency conductivity tensor $\mathbf{C}_L$ measured within the ROIs. The numbers of pixels in the ROIs are shown in the last columns.

(a) MbD-LF-CPI method

	σ_H	$\bar{c}_e$	σ_L	C_{11}	C_{22}	C_{33}	Pixels
CSF	1.19±0.40	0.45 ±0.28	1.18 ±0.40	1.09 ±0.39	1.25 ±0.46	1.19 ±0.44	386
GM	0.55±0.17	0.93 ±0.46	0.33 ±0.21	0.34 ±0.22	0.34 ±0.21	0.32 ±0.22	1576
WM	0.41±0.13	0.87 ±0.40	0.19 ±0.11	0.20 ±0.12	0.18 ±0.11	0.20 ±0.13	2191

(b) three pool method

	σ_H	$\bar{c}_e$	σ_L	C_{11}	C_{22}	C_{33}	Pixels
CSF	1.19±0.40	0.44 ±0.28	1.18 ±0.40	1.10 ±0.39	1.26 ±0.46	1.20 ±0.45	386
GM	0.55±0.17	0.90 ±0.47	0.34 ±0.24	0.34 ±0.24	0.35 ±0.24	0.32 ±0.24	1576
WM	0.41±0.13	0.76 ±0.45	0.21 ±0.11	0.21 ±0.12	0.19 ±0.11	0.21 ±0.14	2191

In order to test the ability of the proposed method for more practical situations, we also used 7 and 4 b-value DWI data. In Fig 4, we compared the recovered extracellular volume fraction α, extracellular mean diffusivity d_w^e, intracellular diffusivity d_w^i, and low-frequency mean conductivity σ_L estimated with all b-value DWIs (15 b-value DWIs), 7 b-value DWIs (b = 300, 500, 700, 1000, 1400, 1800, 3600 s/mm^2), and 4 b-value DWIs (b = 300, 1000, 1800, 3600 s/mm^2) in the first imaging slice of the brain. The 4-th and 5-th columns in Fig 4 show the absolute differences between the corresponding results with 15 and 7 b-value DWIs and those with 15 and 4 b-value DWIs, respectively. Fig 5 shows the recovered results with 15 and 7 b-value DWIs using the three pool method. The differences of reconstructed results with respect to the number of b-values show that the proposed method stably recovers the low-frequency electrical properties with relatively small number of b-value DWIs. The averaged absolute differences (mean and standard deviation) between the corresponding results, α, d_w^e, d_w^i, and σ_L, with 15 and 7 b-value DWIs were 0.03±0.04, 1.48±2.10 × 10^{-4}mm^2/s, 0.58±1.38 × 10^{-4}mm^2/s, and 0.04 ±0.06 S/m, respectively. The averaged absolute differences with 15 and 4 b-value DWIs were 0.05±0.06, 1.58±2.28 × 10^{-4}mm^2/s, 0.73±1.31 × 10^{-4}mm^2/s, and 0.05±0.07 S/m, respectively. On the other hand, in the three pool method, relatively bad values were observed (0.07±0.06, 7.46 ±7.16 × 10^{-4}mm^2/s, 1.00 ±1.58 × 10^{-4}mm^2/s, and 0.10±0.10 S/m, respectively).

We also used the Dice similarity coefficient (DSC) and the relative L^2-error, as our comparison measures. For vectors $\mathbf{a}$ and $\mathbf{b}$, DSC is defined as

$$\text{DSC} = \frac{2\,|\mathbf{a} \cdot \mathbf{b}|}{\|\mathbf{a}\|^2 + \|\mathbf{b}\|^2}. \tag{15}$$

The relative L^2-error is defined as

$$L_{err}^2 = \frac{\|\mathbf{a} - \mathbf{b}\|}{\|\mathbf{a}\|}. \tag{16}$$

For example, in the case of the extracellular volume fraction, $\mathbf{a}$ and $\mathbf{b}$ denote the extracellular volume fractions reconstructed with 15 b-values and sub-sampled b-values, respectively.

Tables 2 and 3 shows the DSC values and the relative L^2-errors between the results with 15 b-value DWIs and sub-sampled b-value DWIs, respectively. For the proposed method compared to the three pool method, higher DSC values and lower relative L^2-errors were reported, especially in the white matter region.
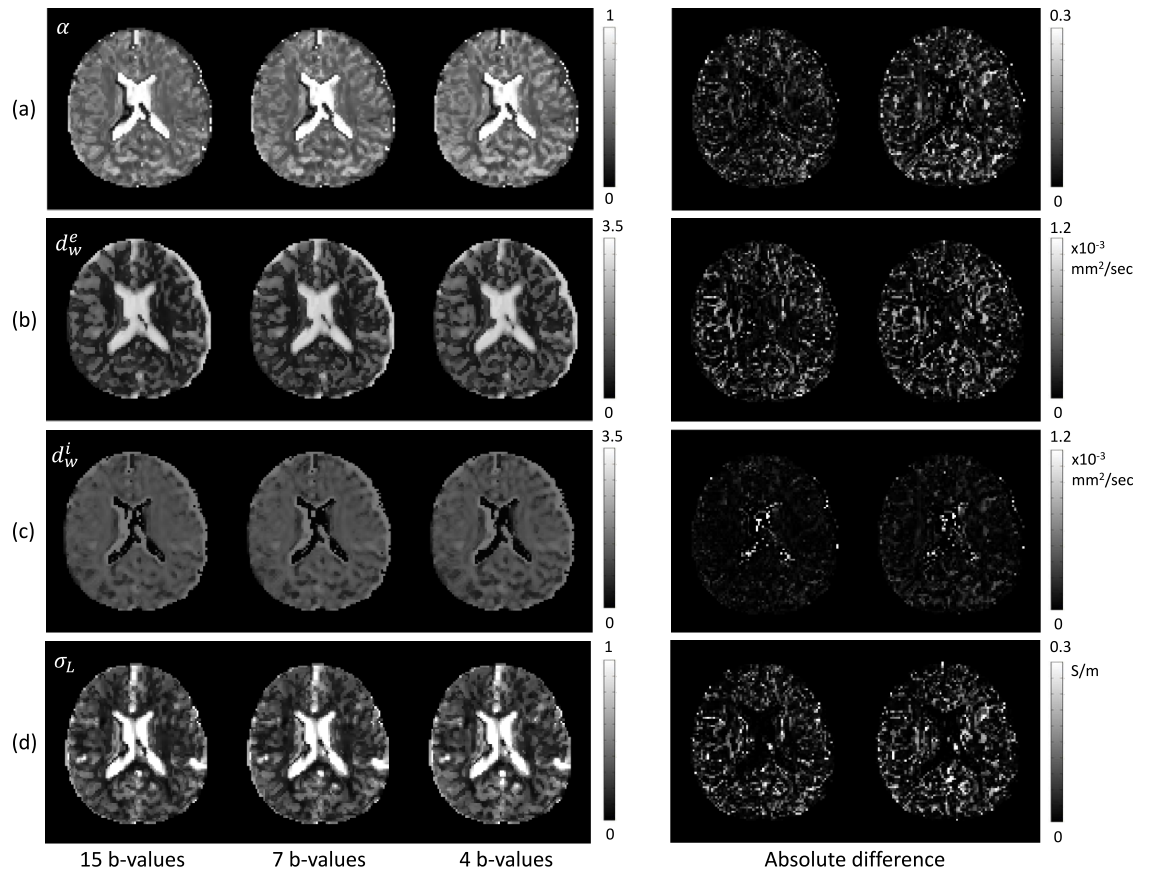
Fig 4. Results of the proposed MbD-LF-CPI method. Comparison of reconstructed results estimated with 15, 7, and 4 b-value DWIs in the first imaging slice of the brain. (a) extracellular volume fraction α, (b) extracellular mean diffusivity d_w^e, (c) intracellular diffusivity d_w^i, and (d) low-frequency mean conductivity σ_L. The 4-th and 5-th columns show the absolute values of difference between the results using 15 b-value DWIs with the results using 7 and 4 b-value DWIs, respectively.

https://doi.org/10.1371/journal.pone.0230903.g004
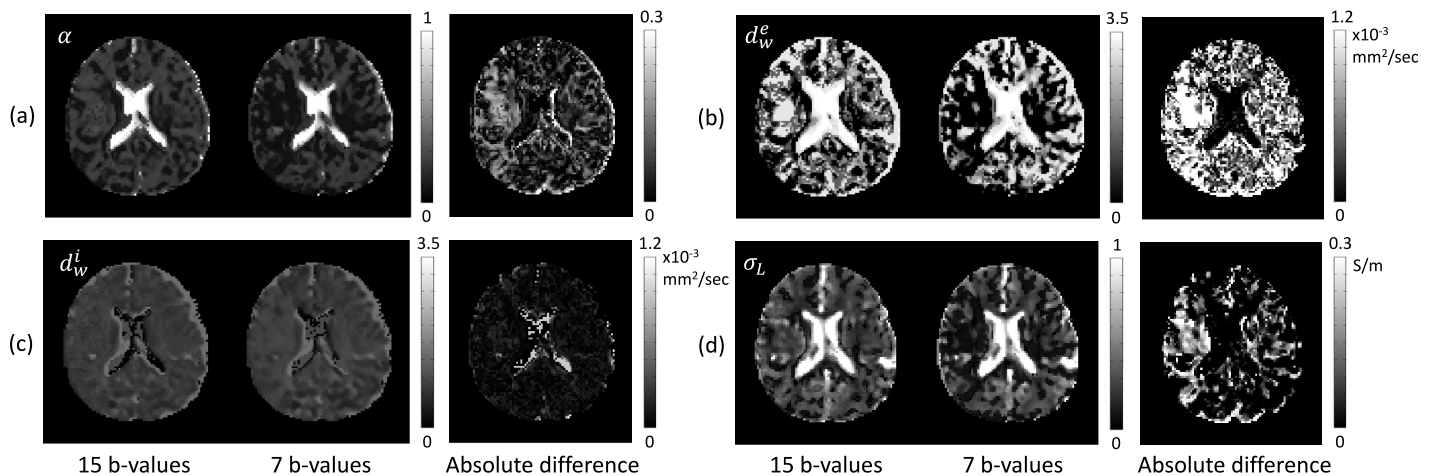
Fig 5. Results of the three pool method. Comparison of reconstructed results estimated with 15 and 7 b-value DWIs in the first imaging slice of the brain. (a) extracellular volume fraction α, (b) extracellular mean diffusivity d_w^e, (c) intracellular diffusivity d_w^i, and (d) low-frequency mean conductivity σ_L. The 3-rd and 6-th columns show the absolute values of difference between the corresponding results with 15 and 7 b-value DWIs, respectively.

https://doi.org/10.1371/journal.pone.0230903.g005

Table 2. DSC values between the results with 15 b-value DWIs and sub-sampled b-value DWIs in the first imaging slice of the brain.

	MbD-LF-CPI method (7 b-values)				MbD-LF-CPI method (4 b-values)				three pool method (7 b-values)			
	Brain	CSF	GM	WM	Brain	CSF	GM	WM	Brain	CSF	GM	WM
α	0.994	0.999	0.992	0.991	0.990	0.998	0.987	0.985	0.958	0.987	0.894	0.893
d_w^e	0.979	0.999	0.976	0.949	0.977	0.999	0.976	0.942	0.912	0.993	0.905	0.884
d_w^i	0.990	0.830	0.999	0.998	0.990	0.862	0.997	0.995	0.976	0.732	0.993	0.993
σ_L	0.990	0.999	0.979	0.972	0.986	0.999	0.970	0.965	0.960	0.994	0.938	0.873

Since there is no available data for the ratio of ion concentrations in ICS and ECS, we used the ratio $\beta = 0.41$ using some reference values [25]. To evaluate the influence of possible errors for β, we recovered the extracellular ion concentration $\bar{c}_e = \frac{\sigma_H}{\alpha d_w^e + (1-\alpha)\beta d_w^i}$ as β was increased from 0.31 to 0.56, respectively. For the true concentration ratio β_t and the assumed $\beta = \beta_t + \beta_\epsilon$, the extracellular concentration $\bar{c}_e$ can be expressed as

$$\bar{c}_e = \frac{\sigma_H}{\alpha d_w^e + (1-\alpha)\beta_t d_w^i} \frac{1}{1 + \dfrac{(1-\alpha)\beta_\epsilon d_w^i}{\alpha d_w^e + (1-\alpha)\beta_t d_w^i}}$$

$$= \bar{c}_e^{true} + \mathcal{O}\left(\frac{(1-\alpha)\beta_\epsilon d_w^i}{\alpha d_w^e + (1-\alpha)\beta_t d_w^i}\right) \qquad (17)$$

where $\bar{c}_e^{true}$ denotes the exact extracellular ion concentration and $g(\epsilon) = \mathcal{O}(\epsilon)$ means that the ratio $\frac{g(\epsilon)}{\epsilon}$ stays bounded as $\epsilon \to 0$. The relation (17) implies that the error between the estimated $\bar{c}_e$ and $\bar{c}_e^{true}$ mainly depends on extracellular volume fraction, extracellular mean diffusivity, and diffusion coefficient d_w^i.

Fig 6 shows the reconstructed apparent extracellular ion concentration $\bar{c}_e$ and low-frequency mean conductivity σ_L as β changes. The second rows of (a) and (b) show the difference between the corresponding results with each β and $\beta = 0.41$, respectively. To compare the corresponding results, we calculated the relative ion concentration changes as

$$Er(\beta) = \frac{|\bar{c}_e(\beta) - \bar{c}_e(\beta = 0.41)|}{\bar{c}_e(\beta = 0.41)}. \qquad (18)$$

The estimated relative ion concentration changes $Er(\beta)$ in the brain region were 0.12, 0.06, 0, 0.05, 0.09, and 0.13 corresponding to $\beta = 0.31, 0.36, 0.46, 0.51,$ and 0.56, respectively. As the ratio of ion concentration varies depending on the tissue structure and pathologic state, as shown in Fig 6, the estimated relative ion concentration changes $Er(\beta)$ in the brain show that

Table 3. Relative L^2-error between the results with 15 b-value DWIs and sub-sampled b-value DWIs in the first imaging slice of the brain.

	MbD-LF-CPI method (7 b-values)				MbD-LF-CPI method (4 b-values)				three pool method (7 b-values)			
	Brain	CSF	GM	WM	Brain	CSF	GM	WM	Brain	CSF	GM	WM
α	0.036	0.023	0.057	0.058	0.075	0.043	0.099	0.107	0.187	0.112	0.342	0.318
d_w^e	0.075	0.023	0.118	0.152	0.090	0.038	0.121	0.212	0.221	0.109	0.315	0.290
d_w^i	0.064	0.411	0.025	0.034	0.062	0.375	0.047	0.058	0.099	0.562	0.072	0.059
σ_L	0.055	0.012	0.134	0.116	0.094	0.034	0.227	0.171	0.171	0.094	0.257	0.353
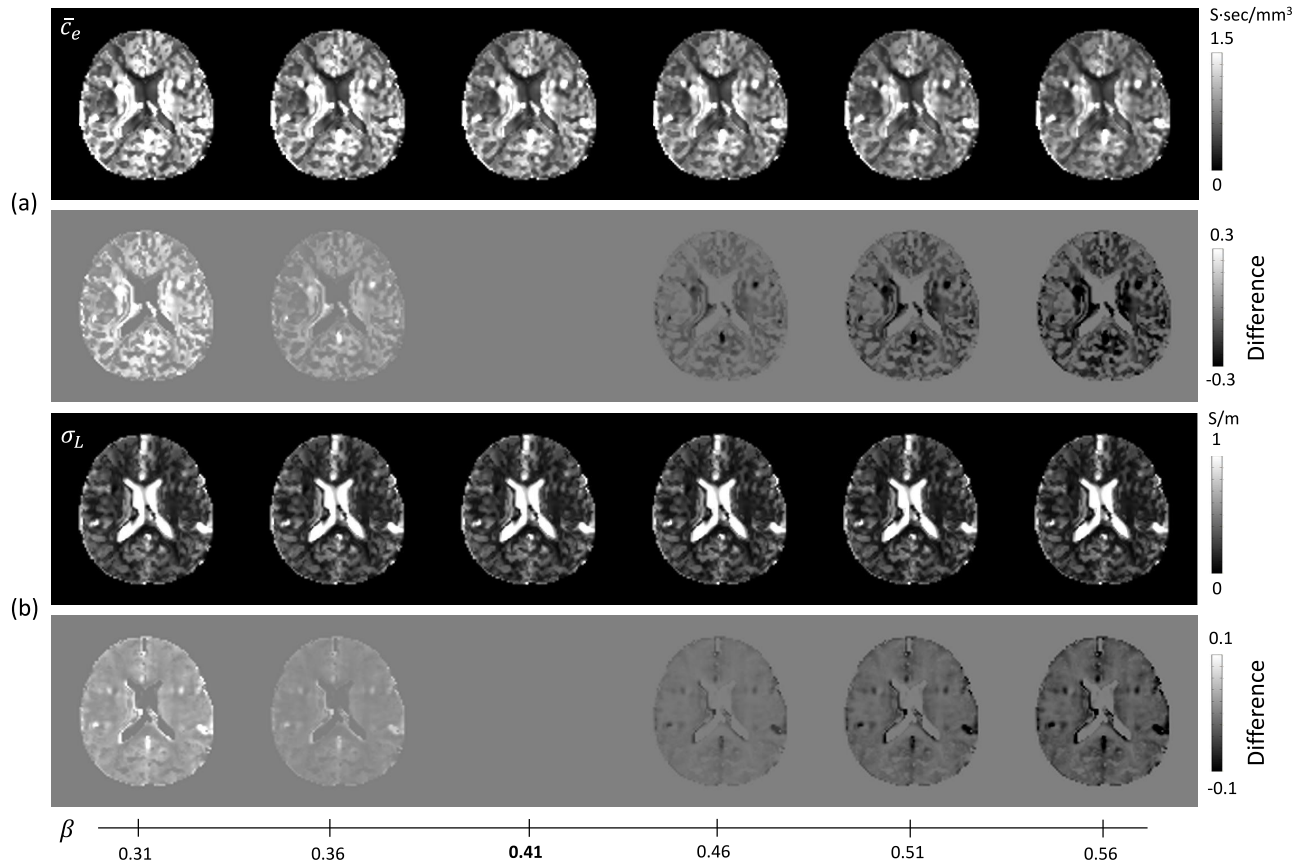
Fig 6. Reconstructed apparent extracellular ion concentration $\bar{c}_e$ and low-frequency mean conductivity σ_L as β changes. (a) Apparent extracellular ion concentration images by changing β value from 0.31 to 0.56 (first row) and the difference images of $\bar{c}_e(\beta) - \bar{c}_e(\beta = 0.41)$ (second row), respectively. (b) Low-frequency conductivity images by changing β value from 0.31 to 0.56 (first row) and the difference images of $\sigma_L(\beta) - \sigma_L(\beta = 0.41)$ (second row), respectively.

https://doi.org/10.1371/journal.pone.0230903.g006

the recovered electrical properties were not significantly sensitive to the slightly changed β for the fixed $\beta = 0.41$.

In Fig 7, we compared the recovered extracellular volume fraction α, extracellular diffusivity d_w^e, intracellular diffusivity d_w^i, and low-frequency mean conductivity σ_L estimated with 15 gradient directions and 3 orthogonal gradient directions in the first imaging slice of the brain. The 3-rd and 6-th columns in Fig 7 show the absolute differences between the corresponding results with 15 and 3 gradient directions, respectively. The relative L^2-errors of α, d_w^e, d_w^i, and σ_L with 15 and 3 gradient directions were 0.032, 0.048, 0.049, and 0.069, respectively. Here, the relative L^2-errors were calculated using (16). **a** and **b** in (16) mean the values reconstructed with 15 gradient directions and 3 orthogonal gradient directions, respectively. For the three pool method, the corresponding relative L^2-errors were 0.042, 0.072, 0.060, and 0.084.

Discussion

To extract the low-frequency conductivity information from the high-frequency conductivity, we decomposed the recovered high-frequency conductivity by using MREPT technique from B1 phase measurements into a weighted combination of the conductivity of intracellular and extracellular compartments. The DWI for a fixed b-value assumes that all water molecules in a voxel have a single ADC, the ADC, however, reflects combined diffusion properties of
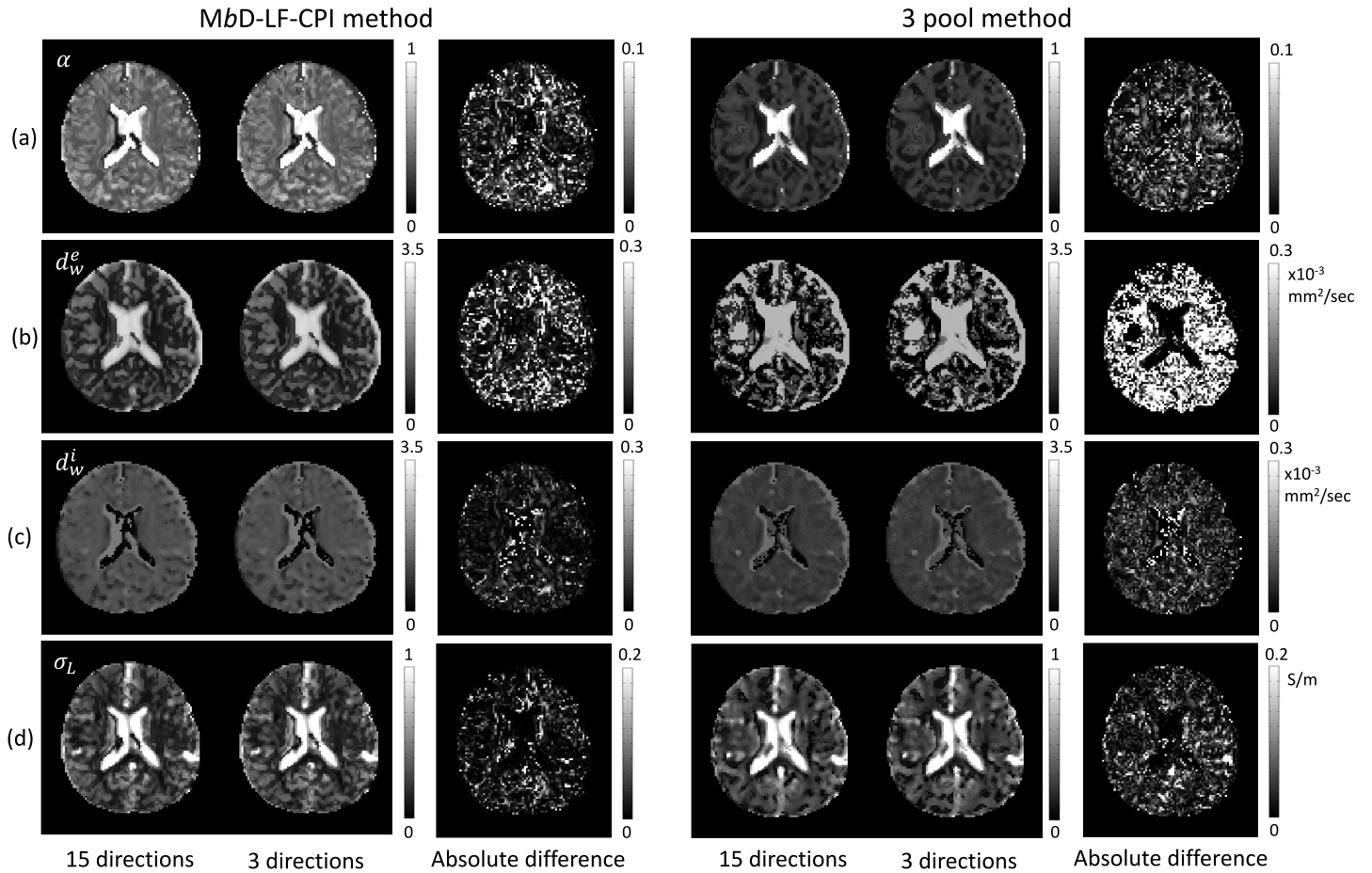
Fig 7. Comparison of reconstructed results estimated with 15 gradient directions and 3 orthogonal gradient directions in the first imaging slice of the brain. (a) extracellular volume fraction α, (b) extracellular mean diffusivity d_w^e, (c) intracellular diffusivity d_w^i, and (d) low-frequency mean conductivity σ_L. The 3-rd and 6-th columns show the absolute values of difference between the corresponding results with 15 and 3 gradient directions, respectively.

intracellular and extracellular compartments. Multi-b value DWIs with multi-diffusion gradient directions have been widely studied to detect multi-diffusion coefficient and the intracellualr and extracellular volume fractions [23]. The water diffusion in ECS is less restricted and hindered than that in ICS. The b-value is a key parameter in the water diffusion and high b-values have been known to be more sensitive to ICS [32]. We found that the estimated low-frequency conductivity tensor using the proposed method was slightly low in the white matter region because the white matter was highly anisotropic due to the parallel orientation of the nerve fiber tracts.

To estimate the low-frequency electrical properties in ECS, we designed the multi-compartment model (7). The developed model estimated the microstructure of ICS reflected the averaged intracellular diffusion coefficient d_{ic} = 1.7 mm^2/s and volume fraction v_{ic}, the extracellular diffusivity, and CSF compartment (diffusion coefficient d_{iso} = 3 mm^2/s and volume fraction v_{iso}). The proposed method used several DWI signals for different b-values to recover the low-frequency conductivity in the brain region, the recovered volume fraction in ECS was, however, overestimated because the recovered extracellular microstructure still included unmyelinated neurons and other cells of the central nervous system. The hindered diffusion of free water molecules, related to the intrinsic diffusion coefficient of extracellular

space and the tortuosity of the tissue, makes it difficult to distinguish the diffusion in the intra-cellular space, depending on the cell structures. To precisely estimate the low-frequency con-ductivity using only an MRI scanner, a new model for DWI to detect the diffusion-limited compartment and more exact estimation of microstructures in ECS are needed in the future work.

The proposed method recovers the ion concentration and the mean mobility in ECS using multi-b-value DWIs. In this paper, we focused on the reconstruction of the low-frequency con-ductivity tensor as a 3×3 positive definite symmetric matrix form. Due to the anisotropic con-ductivity tensor, the recovered low-frequency conductivity can be used to predict the current pathway and electric field distribution, which could be useful information for proving the ther-apeutic effects of electrical stimulation. Electrical brain stimulation (EBS) techniques are promising treatments for human disorders: transcranial direct current stimulation (tDCS), cranial electrotherapy stimulation (CES), electroconvulsive therapy (ECT), and deep brain stimulation (DBS), etc. EBS studies have relied on computational modeling using known refer-ence conductivity values in the brain and thus the specificity of each individual's brain is an obstacle of EBS. The proposed method can provide a way to investigate the EBS without real experiments.

DTI is currently a widely used technique for visualizing major fiber orientation of the brain in fitting a Gaussian distribution of diffusion, but DTI also has limitations in characterizing the diffusion process in areas of low anisotropy and complex fiber structure in a voxel. Using a higher number of diffusion gradient directions, various techniques have been introduced to overcome the limitation of DTI [5]. Although high angular methods use more gradient encod-ing directions and high gradient strength (b-value) than DTI, we believe that anisotropic elec-trical properties also can be extended to characterize the complex anisotropy depending on the fiber structures in a voxel.

We expect that the recovered concentration image can be applied to the relevant diseases. There are many diseases related to ion channels: physiological disorders (myotonias, Brugada syndrome, malignant hyperthermia, myasthenia), neuronal disorders (epilepsy and episodic ataxia, retinal diseases, Alzheimer's disease, Parkinson's disease, schizpphrenia), kidney disor-ders (policystic kidney disease, hyperinsulinemic hypoglycemia of infancy and cystic fibrosis, congenital stationary night blindness), etc. [33, 34]. Hence, rigorous analysis of the ion con-centration characteristics by using a noninvasive imaging modality such as MRI is crucial to the pathophysiolgy of neurodegenerative processes.

Conclusion

The water diffusion weighted imaging (DWI) measures the random Brownian motion of water molecules within a voxel, which related to the mobility of the water molecules by the Einstein relation. We investigated the decomposed high-frequency conductivity as the appar-ent total ion concentration and the mobility terms. MREPT uses the B1 mapping technique to provide the high-frequency conductivity distribution that reflects the intracellular and extra-cellular effects at the Larmor frequency of an MRI scanner. By measuring DWI data for multi-b-value and the recovered high-frequency conductivity distribution, we proposed a new multi-compartment model to estimate the extracellular volume fraction, the extracellular mean diffu-sivity, and the volume fraction of CSF. Using the estimated parameters, the high-frequency conductivity is decomposed into the apparent ion concentration and the extracellular mean mobility. A human experiment verified that the proposed method has the potential to rapidly recover the low-frequency electrical properties without any additional external injection current.

Supporting information

S1 Fig. Recovered results. (a) Recovered high-frequency conductivity σ_H. (b) Recovered extracellular volume fraction α, extracellular mean diffusivity d_w^e, intracellular diffusivity d_w^i, the apparent extracellular ion concentration $\bar{c}_e$ and low-frequency mean conductivity σ_L images, respectively, using MbD-LF-CPI method. (c) Recovered results corresponding to (b) using the three pool model method.
(EPS)

S2 Fig. Diffusion and conductivity tensors. (a) Water molecule diffusion tensor using the b value of 1000 s/mm^2 in the first slice. (b) Reconstructed low-frequency conductivity tensor images using MbD-LF-CPI method. (c) Reconstructed low-frequency conductivity tensor images using the three pool model.
(EPS)

S1 Table. Results of the proposed MbD-LF-CPI method and the three pool method. Estimated high-frequency conductivity σ_H, extracellular ion concentration $\bar{c}_e$, low-frequency mean conductivity σ_L, diagonal components of reconstructed low-frequency conductivity tensor $\mathbf{C}_L$ measured within the ROIs.
(PDF)

Acknowledgments

Author Contributions

Conceptualization: Mun Bae Lee, Eung Je Woo.

Data curation: Mun Bae Lee, Geon-Ho Jahng, Hyung Joong Kim.

Methodology: Mun Bae Lee.

Project administration: Oh In Kwon.

Validation: Geon-Ho Jahng, Eung Je Woo.

Writing – original draft: Oh In Kwon.

Writing – review & editing: Mun Bae Lee, Geon-Ho Jahng, Hyung Joong Kim, Eung Je Woo.

References

1. Gabriel S, Lau R, Gabriel C. The dielectric properties of biological tissues: II. Measurements in the frequency range 10 Hz to 20 GHz. Physics in medicine & biology. 1996; 41(11):2251. https://doi.org/10.1088/0031-9155/41/11/002

2. Woo EJ, Seo JK. Magnetic resonance electrical impedance tomography (MREIT). SIAM Rev. 2011; 53:40–68. https://doi.org/10.1137/080742932

3. Kwon OI, Jeong WC, Saurav ZKS, Kim HJ, Woo EJ. Anisotropic conductivity tensor imaging in MREIT using directional diffusion rate of water molecules. Phys Med Biol. 2014; 59:2955–2974. https://doi.org/10.1088/0031-9155/59/12/2955 PMID: 24841854

4. Scott GC, Joy MLG, Armstrong RM. Measurement of nonuniform current density by magnetic resonance. IEEE Trans Med Imag. 1991; 10:362–374. https://doi.org/10.1109/42.97586

5. Tuck DS, Wedeen VJ, Dale AM, George JS, Belliveau JW. Conductivity tensor mapping og the human brain using diffusion tensor MRI. Proc Natl Acad, Sci. 2001; 98:11697–11701. https://doi.org/10.1073/pnas.171473898

6. Gurler N, Ider YZ. Gradient-based electrical conductivity imaging using MR phase. Magnetic resonance in medicine. 2017; 77(1):137–150. https://doi.org/10.1002/mrm.26097 PMID: 26762771

7. Katscher U, Voigt T, Findeklee C, Vernickel P, Nehrke K, Doessel O. Determination of electric conductivity and local SAR via B1 mapping. IEEE transactions on medical imaging. 2009; 28(9):1365–1374. https://doi.org/10.1109/TMI.2009.2015757 PMID: 19369153

8. Miklavčič D, Pavšelj N, Hart FX. Electric properties of tissues. Wiley encyclopedia of biomedical engineering. 2006.

9. Gabriel C, Peyman A, Grant E. Electrical conductivity of tissue at frequencies below 1 MHz. Physics in medicine & biology. 2009; 54(16):4863. https://doi.org/10.1088/0031-9155/54/16/002

10. Ider YZ, Birgül Ö. Use of the magnetic field generated by the internal distribution of injected currents for electrical impedance tomography (MR-EIT). Turkish Journal of Electrical Engineering & Computer Sciences. 2000; 6(3):215–226.

11. Park C, Lee BI, Kwon OI. Analysis of recoverable current from one component of magnetic flux density in MREIT and MRCDI. Phys Med Biol. 2007; 52(1):3001–3013. https://doi.org/10.1088/0031-9155/52/11/005 PMID: 17505085

12. Hamamura MJ, Muftuler LT. Fast imaging for magnetic resonance electrical impedance tomography. Magnetic resonance imaging. 2008; 26(6):739–745. https://doi.org/10.1016/j.mri.2008.01.031 PMID: 18499381

13. Seo JK, Yoon JR, Woo EJ, Kwon O. Reconstruction of conductivity and current density images using only one component of magnetic field measurements. IEEE Transactions on Biomedical Engineering. 2003; 50(9):1121–1124. https://doi.org/10.1109/TBME.2003.816080 PMID: 12943280

14. Kim HJ, Kim YT, Minhas AS, Jeong WC, Woo EJ, Seo JK, et al. In vivo high-resolutionconductivity imaging of the human leg using MREIT: the first human experiment. IEEE transactions on medical imaging. 2009; 28(11):1681–1687. https://doi.org/10.1109/TMI.2009.2018112 PMID: 19369151

15. Jeong WC, Sajib SZK, Katoch N, J KH, Kwon OI, Woo EJ. Anisotropic conductivity tensor imaging of in vivo canine brain using DT-MREIT. IEEE Trans Med Imag. 2017; 36:124–131. https://doi.org/10.1109/TMI.2016.2598546

16. Voigt T, Katscher U, Doessel O. Quantitative conductivity and permittivity imaging of the human brain using electric properties tomography. Magnetic Resonance in Medicine. 2011; 66(2):456–466. https://doi.org/10.1002/mrm.22832 PMID: 21773985

17. Lee J, Shin J, Kim DH. MR-based conductivity imaging using multiple receiver coils. Magnetic resonance in medicine. 2016; 76(2):530–539. https://doi.org/10.1002/mrm.25891 PMID: 26375762

18. Park JA, Kang KJ, Ko IO, Lee KC, Choi BK, Katoch N, et al. In Vivo Measurement of Brain Tissue Response after Irradiation: Comparison of T2 Relaxation, Apparent Diffusion Coefficient, and Electrical Conductivity. IEEE transactions on medical imaging. 2019. https://doi.org/10.1109/TMI.2019.2913766

19. Selimbeyoglu A, Parvizi J. Electrical stimulation of the human brain: perceptual and behavioral phenomena reported in the old and new literature. Frontiers in human neuroscience. 2010; 4.

20. Le Bihan D, Urayama S, Aso T, Hanakawa T, Fukuyama H. Direct and fast detection of neuronal activation in the human brain with diffusion MRI. Proceedings of the National Academy of Sciences. 2006; 103(21):8263–8268. https://doi.org/10.1073/pnas.0600644103

21. Le Bihan D. Intravoxel incoherent motion perfusion MR imaging: a wake-up call. Radiology. 2008; 249 (3):748–752. https://doi.org/10.1148/radiol.2493081301 PMID: 19011179

22. Le Bihan D, Breton E, Lallemand D, Grenier P, Cabanis E, Laval-Jeantet M. MR imaging of intravoxel incoherent motions: application to diffusion and perfusion in neurologic disorders. Radiology. 1986; 161 (2):401–407.

23. Zhang H, Schneider T, Wheeler-Kingshott CA, Alexander DC. NODDI: practical in vivo neurite orientation dispersion and density imaging of the human brain. Neuroimage. 2012; 61(4):1000–1016. https://doi.org/10.1016/j.neuroimage.2012.03.072 PMID: 22484410

24. Westin CF, Knutsson H, Pasternak O, Szczepankiewicz F, Özarslan E, van Westen D, et al. Q-space trajectory imaging for multidimensional diffusion MRI of the human brain. NeuroImage. 2016; 135:345–362. https://doi.org/10.1016/j.neuroimage.2016.02.039 PMID: 26923372

25. Sajib SZ, Kwon OI, Kim HJ, Woo EJ. Electrodeless conductivity tensor imaging (CTI) using MRI: basic theory and animal experiments. Biomedical Engineering Letters. 2018; 8:273–282. https://doi.org/10.1007/s13534-018-0066-3 PMID: 30603211

26. Katoch N, Choi BK, Sajib SZ, Lee EA, Kim HJ, Kwon OI, et al. Conductivity Tensor Imaging of In Vivo Human Brain and Experimental Validation using Giant Vesicle Suspension. IEEE Transactions on Medical Imaging. 2018. https://doi.org/10.1109/TMI.2018.2884440 PMID: 30507528

27. Jeurissen B, Tournier JD, Dhollander T, Connelly A, Sijbers J. Multi-tissue constrained spherical deconvolution for improved analysis of multi-shell diffusion MRI data. NeuroImage. 2014; 103:411–426. https://doi.org/10.1016/j.neuroimage.2014.07.061 PMID: 25109526

28. Daducci A, Canales-Rodríguez EJ, Zhang H, Dyrby TB, Alexander DC, Thiran JP. Accelerated micro-structure imaging via convex optimization (AMICO) from diffusion MRI data. Neuroimage. 2015; 105:32–44. https://doi.org/10.1016/j.neuroimage.2014.10.026 PMID: 25462697

29. Pierpaoli C, Jones D. Removing CSF contamination in brain DT-MRIs by using a two-compartment tensor model. In: International Society for Magnetic Resonance in Medicine Meeting; 2004. p. 1215.

30. Mansfield P. Multi-planar image formation using NMR spin echoes. Journal of Physics C: Solid State Physics. 1977; 10(3):L55. https://doi.org/10.1088/0022-3719/10/3/004

31. Kwon OI, Jeong WC, Sajib SZ, Kim HJ, Woo EJ, Oh TI. Reconstruction of dual-frequency conductivity by optimization of phase map in MREIT and MREPT. Biomedical engineering online. 2014; 13(1):24. https://doi.org/10.1186/1475-925X-13-24 PMID: 24607262

32. Assaf Y, Ben-Bashat D, Chapman J, Peled S, Biton I, Kafri M, et al. High b-value q-space analyzed diffusion-weighted MRI: application to multiple sclerosis. Magnetic Resonance in Medicine. 2002; 47 (1):115–126. https://doi.org/10.1002/mrm.10040 PMID: 11754450

33. Dworakowska B, Dolowy K. Ion channels-related diseases. Acta Biochimica Polonica. 2000; 47:685–703. https://doi.org/10.18388/abp.2000_3989 PMID: 11310970

34. Hübner CA, Jentsch TJ. Ion channel diseases. Human molecular genetics. 2002; 11(20):2435–2445. https://doi.org/10.1093/hmg/11.20.2435 PMID: 12351579